Supplementary Information

Solution-Processed Single-Component Organic Photodetectors - Strong Quadrupole Moments in Molecules Enable the State-of-the-Art Performance

Song Yi Park[1,†], Chiara Labanti[1,†], Tack Ho Lee[2], Richard A. Pacalaj[2], Yifan Dong[2], Yi-Chun Chin[1], Joel Luke[1], Gihan Ryu[1], Daiki Minami[3], Sungyoung Yun[4], Jeong-Il Park[4], Feifei Fang[4], and Kyung-Bae Park[4], James R. Durrant[2,5], and Ji-Seon Kim[1,*]

[1]Department of Physics and Centre for Processable Electronics, Imperial College London, London SW7 2AZ, UK
E-mail: ji-seon.kim@imperial.ac.uk

[2]Department of Chemistry and Centre for Processable Electronics, Imperial College London, White City Campus, London W12 0BZ, UK

[3]CSE team, Innovation Center, Samsung Electronics, Co. Ltd., 1 Samsungjeonja-ro, Hwasung-si, Gyeonggi-do 18448, Republic of Korea

[4]Organic Materials Lab, Samsung Advanced Institute of Technology, Samsung Electronics Co. Ltd., Samsung-ro, Yeongtong-gu, Suwon-si, Gyeonggi-do, 16678, Korea

[5]SPECIFIC IKC, Faculty of Science and Engineering, Swansea University, SA2 7AX, United Kingdom

[†]These authors contributed equally to this work.

Experimental Methods

General: IDIC, O-IDFBR, Y6 and IT-4F were purchased from Solarmer Materials. Absorbance data were obtained using a Shimadzu UV-2550 UV–vis spectrophotometer. Ambient photoemission spectroscopy (APS) was measured by an APS04 Air Photoemission system (KP Technology) using a 2 mm gold tip in ambient conditions. The same equipment was used for surface photovoltage (SPV) analysis of NFA/ZnO/ITO samples. SPV was quantified as the changes in surface potential in dark and illuminated conditions using a white bulb light source, with tunable intensity up to 1/5 Sun.

Device fabrication procedures and characterization: OPD devices were prepared with a structure of glass/indium tin oxide (ITO)/ZnO/NFA/MoO_x/Ag. Pre-patterned ITO on glass substrates were cleaned by ultra-sonication with deionized water, acetone, and 2-propanol. The substrates were then dried in an oven at 80 °C overnight. ZnO layer was prepared by sol−gel method (dissolving zinc acetate in 2-methoxyethanol with 3 vol % ethanolamine solution). After surface treatment of ITO by O_2 plasma ashing, ZnO solution was coated on the ITO substrates and thermally annealed at 190 °C for 20 minutes. IDIC, O-IDFBR, Y6 and IT-4F solutions were prepared in chloroform (CF) with 10 mg/mL concentration and stirred overnight at 40 °C prior to spin casting. After spin-coating the NFA layer on top of the ZnO substrates, the samples were brought into a high vacuum chamber (~10^{-6} Torr), and MoO_x (10 nm) and Ag (100 nm) was deposited sequentially by thermal evaporation. Device area was 6.0 mm^2. Measurements were conducted outside the glovebox, and the devices were stored in a nitrogen filled chamber. Solar simulator was used for 1 Sun measurement which intensity was calibrated at 100 mW cm^{-2} with a standard silicon photodiode. Light intensities were modulated using neutral density filters. Current density-voltage (*J-V*) characteristics were measured with a Keithley 2400 source measurement unit. The photocurrent transients were obtained with a DAQ card connected to a Tektronix TDS3032B Oscilloscope. External quantum efficiency (EQE) was measured using an EQE system of a tungsten halogen lamp coupled with a grating spectrometer (CS260-RG-4-MT-D). PL spectra were measured by a Renishaw inVia Raman microscope in backscattering configuration, with a 514 nm laser (Argon, Titanium Sapphire lasers). The samples were kept under nitrogen in a custom-designed chamber to reduce degradation effects. Laser spot diameter was of the order of 10 μm, 25% defocused on the sample, and diffracted light was separated by a diffraction grid (300 lines/mm). A Si reference

sample was used for spectrometer calibration. Optimized acquisition parameters (laser power, exposure time, measurement accumulation number) were kept consistent for the same experiments. Accuracy was improved by checking the reproducibility of spectra over multiple positions on the surface. PL was also measured on encapsulated devices applying reverse bias to the electrodes using a Keithley 2400 or Agilent voltage source. Time-correlated single photon counting (TCSPC) on thin films (on quartz) or solutions was measured in air by a photoluminescence spectrometer (FLS1000, Edinburgh Instruments), following sample excitation by lasers of different wavelengths (405 nm for O-IDTBR and 800 nm for Y6). Lifetimes are extracted by multi-exponential fitting using FAST software.

Transient absorption spectroscopy: Helios spectrometer (Spectra Physics, Newport Corp.) was used to measure the broadband pump-probe femtosecond TAS and kinetics for thin film samples. Ultrafast laser pulses (800 nm, 100 fs duration) were generated by a 1 kHz Ti:sapphire regenerative amplifier (Solstice, Spectra Physics, Newport Corp.). One portion of the 800 nm pulse was directed to an optical parametric amplifier (TOPAS Prime, Spectra-Physics) and a frequency mixer (Niruvis, Light Conversion) to tune the visible pump pulses at various wavelengths. The pump pulses were modulated at a frequency of 500 Hz by a mechanical chopper. The rest of the 800 nm pulse was routed onto a mechanical delay stage with a 6 ns time window and directed through a non-linear sapphire crystal (sapphire for the visible region and YAG for the NIR region) to generate a white light probe ranging for the visible region from 400 to 1600 nm. The probe pulse was split into two by a neutral density filter. One portion of the probe pulse served as the reference and was directly sent to the fiber-optic coupled multichannel spectrometers (CCD and InGaAs sensors). The rest of the probe pulse together with the pump pulse were focused onto the same spot on the samples with a beam size of around 0.5 mm^2 before sending it to the spectrometer. To compensate the fluctuations, the measured spectrum was normalized to the reference spectrum and averaged for several scans to achieve a good signal-to-noise ratio. Data analysis was performed with the commercialized Surface Xplorer software.

Simulation: Optimized packing structures of face-on and edge-on were obtained by DFT calculations for 4 molecules placed in a cell with periodic boundary conditions. The DFT calculations were carried out using Vienna ab initio simulation package (VASP)[1–5] under the conditions of flexible cell (the shape and size of cell can be changed during the structure

optimization). The interface morphology between face-on and edge-on packings was generated from the crystal structures[6,7] and the morphology was relaxed through energy minimization with the molecular dynamics (MD) force field using Desmond package (Schrödinger, LLC, NY, USA)[8]. Here, we employed optimized potentials for liquid simulations (OPLS) as the force field which is widely used for MD simulation of organic molecules. The dimer structures extracted from the face-on packing structures and the interface between face-on and edge-on packings which was obtained by the DFT and MD energy minimization as explained above. The electronic excited state ($S_1 - S_4$) of the dimer structures were calculated by time-dependent DFT (TD-DFT) using Jaguar package (Schrödinger, LLC, NY, USA)[9] with basis sets of b3lyp/6-31G**.

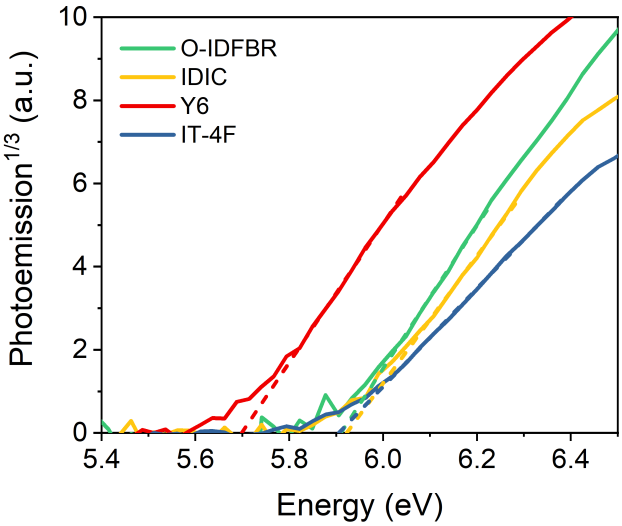

Supplementary Figure 1. Ambient photoemission spectra to determine HOMO level of NFA neat films. Measured HOMO levels are -5.92, -5.91, -5.91, -5.70, and -5.91 eV for O-IDFBR, IDIC, Y6, and IT-4F films, respectively.

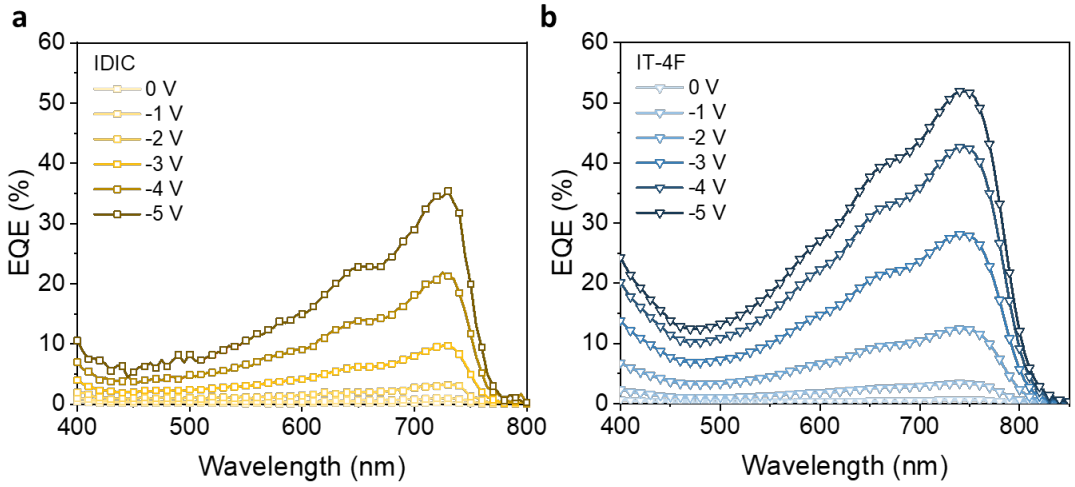

Supplementary Figure 2. Bias external quantum efficiency (EQE) spectra for **a**, IDIC and **b**, IT-4F OPDs.

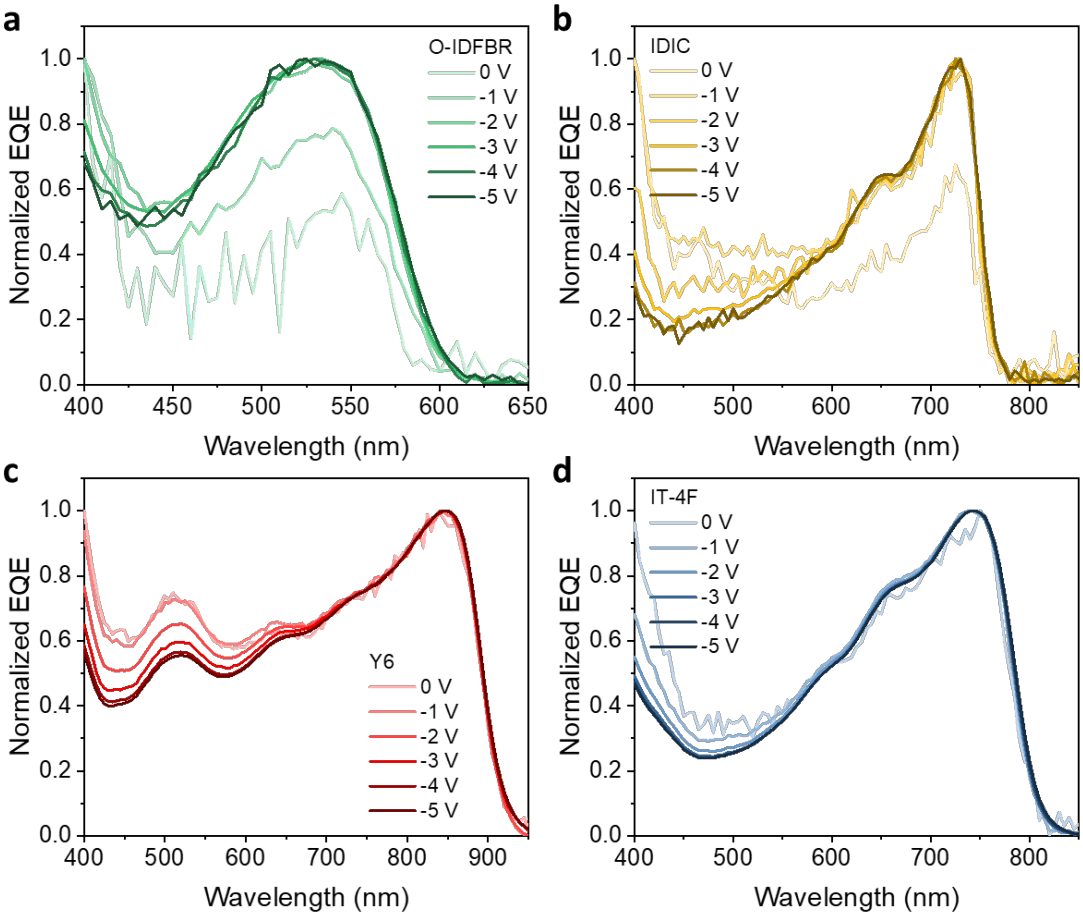

Supplementary Figure 3. Normalized EQE spectra of **a**, O-IDFBR, **b**, IDIC, **c**, Y6 and **d**, IT-4F OPDs with applying reverse bias from 0 to -5 V.

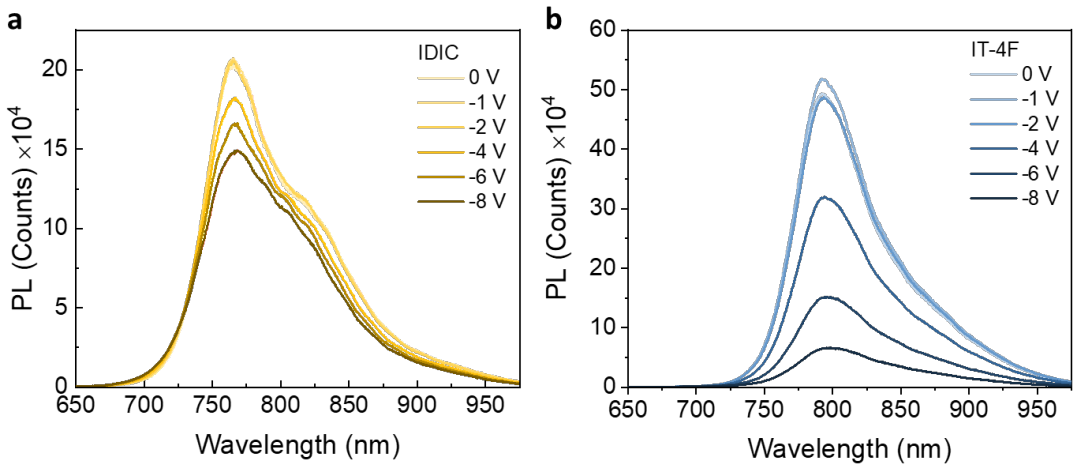

Supplementary Figure 4. Bias photoluminescence (PL) spectra of **a**, O-IDFBR and **b**, IT-4F OPDs.

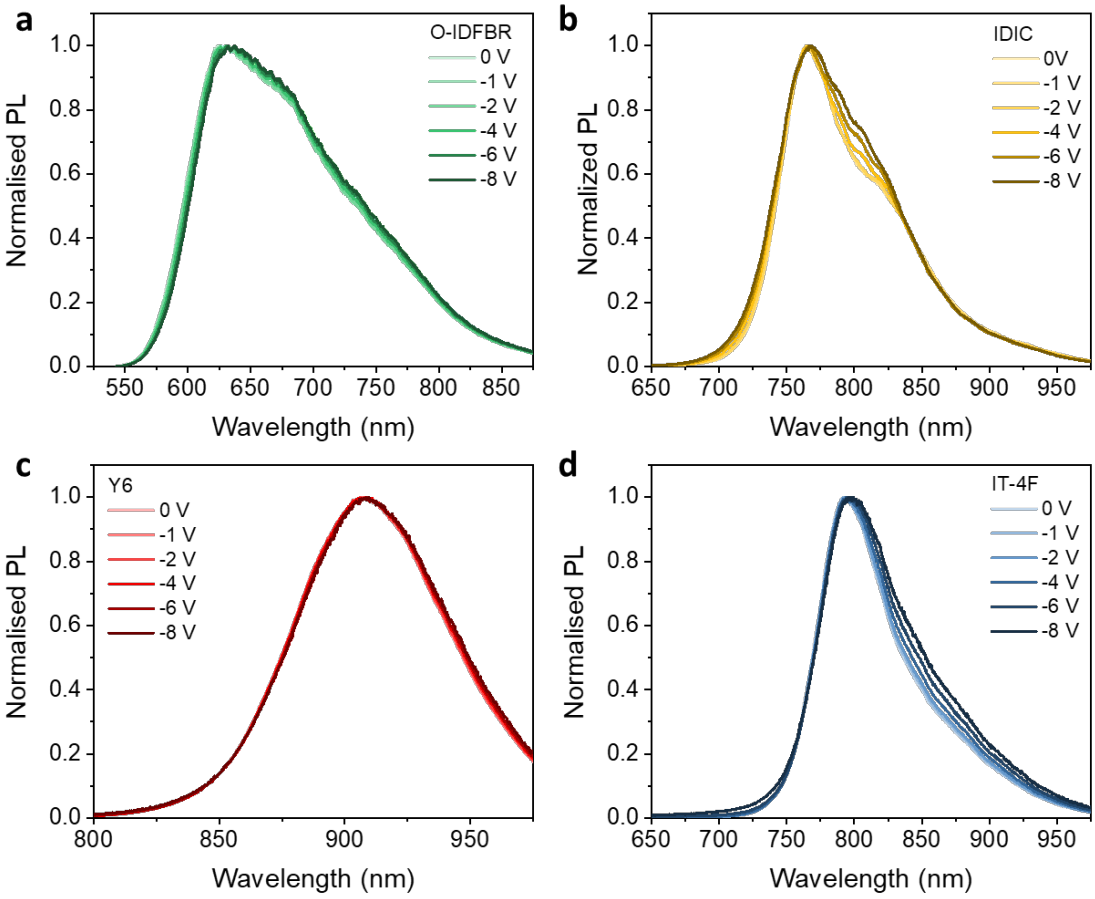

Supplementary Figure 5. Normalized PL spectra of **a**, O-IDFBR, **b**, IDIC, **c**, Y6 and **d**, IT-4F OPDs with applying reverse bias from 0 to -5 V.

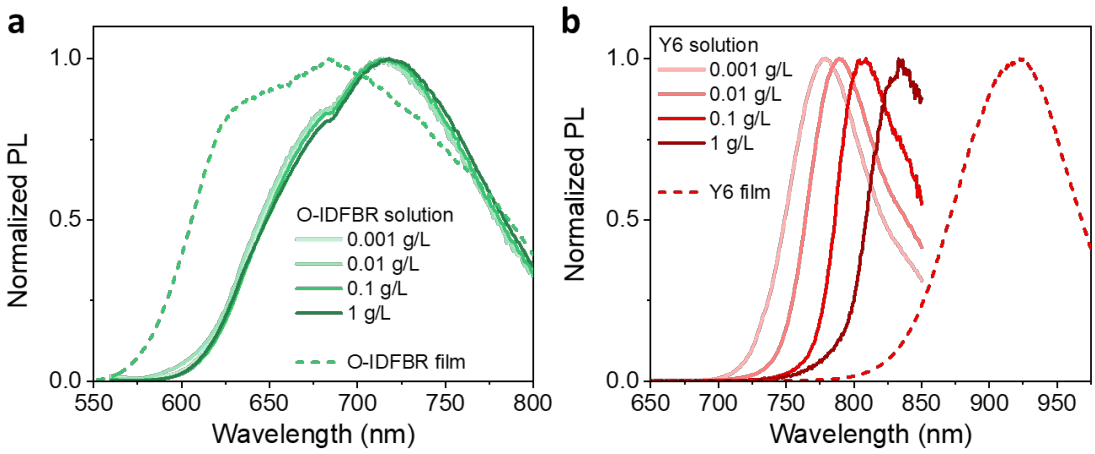

Supplementary Figure 6. PL spectra of **a**, O-IDFBR and **b**, Y6 in solution (indicated to the concentration) and film states.

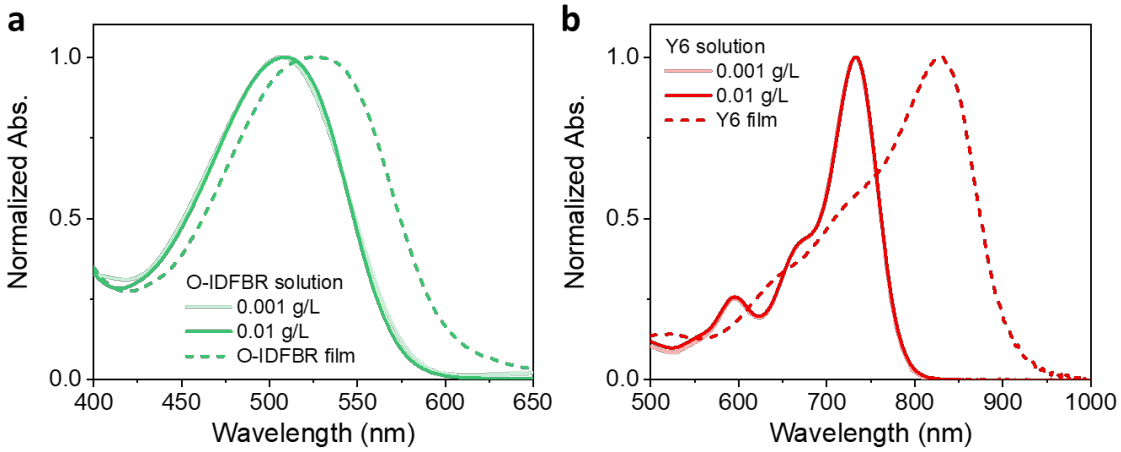

Supplementary Figure 7. Absorption spectra of **a**, O-IDFBR and **b**, Y6 in solution (indicated to the concentration) and film states.

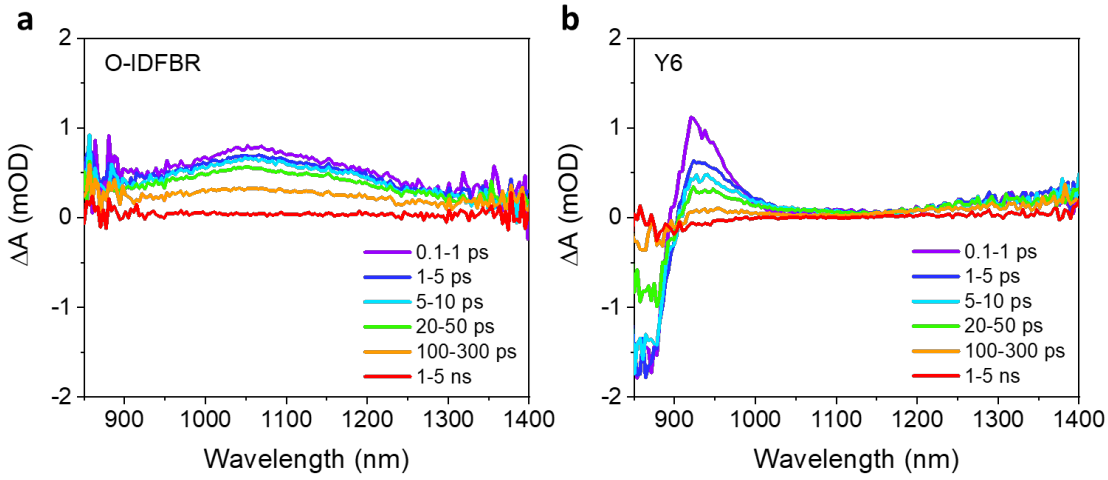

Supplementary Figure 8. a, Transient absorption spectra of O-IDFBR neat film with energy density of 5 μJ cm^{-2} excited at 380 nm. **b**, Transient absorption spectra of Y6 neat film with energy density of 5 μJ cm^{-2} excited at 750 nm. Probed kinetics at 1060 and 930 nm for O-IDFBR and Y6, respectively, are shown in **Fig.4**.

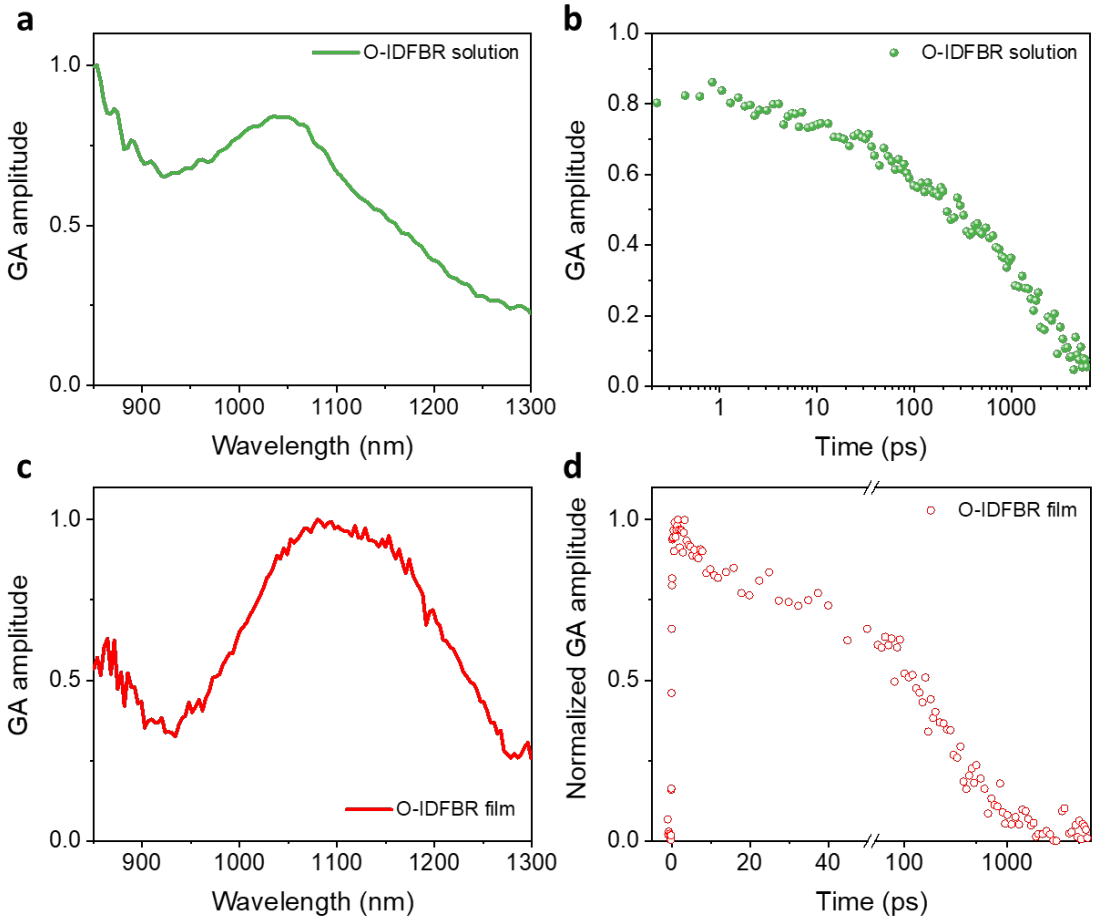

Supplementary Figure 9. Global analyses results for the TA data for O-IDFBR in Figure 8. All data could be fitted to one component; inclusion of a second component in the fit did not resolve a kinetically distinguishable species. Deconvoluted **a,** spectra and **b**, kinetics for O-IDFBR solution. Deconvoluted **c**, spectra and **d**, kinetics for O-IDFBR film.

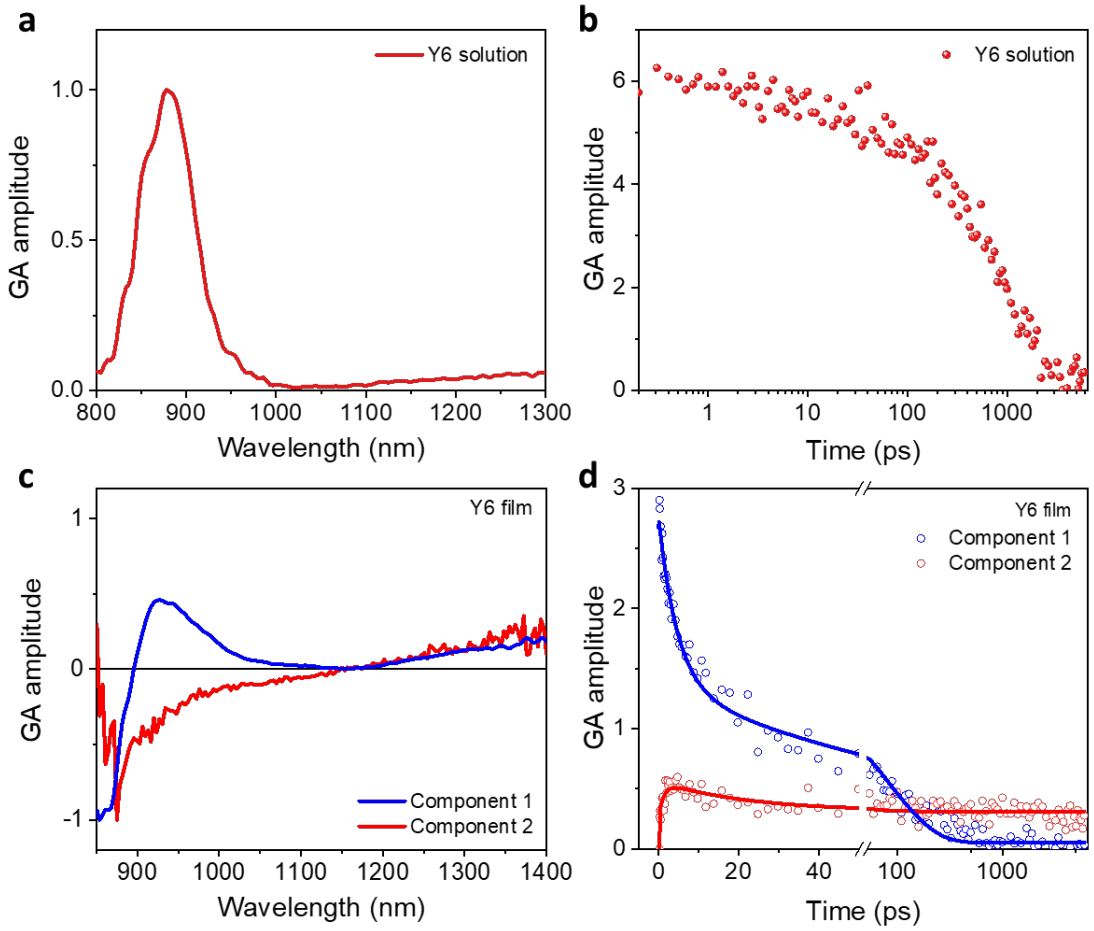

Supplementary Figure 10. Global analyses results for the TA data for Y6 in Figure 8. For solution Y6, the data could be fitted to one component; inclusion of a second component in the fit did not resolve a kinetically distinguishable species. For Y6, two components were required to fit the data, as shown. Deconvoluted **a,** spectra and **b**, kinetics for Y6 solution. Deconvoluted **c**, spectra and **d**, kinetics for Y6 film.

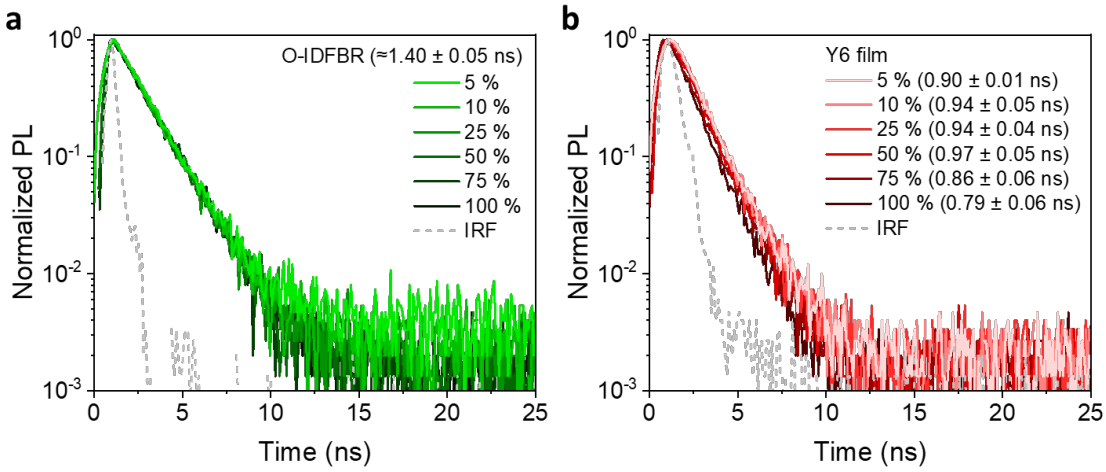

Supplementary Figure 11. Excitation light intensity dependent TCSPC kinetics for film of **a**, O-IDFBR (excitation λ = 405 nm, probe λ = 625 nm) and **b**, Y6 (excitation λ = 800 nm, probe λ = 900 nm). Light intensity is indicated as percentage of maximum laser intensity (with a photon flux of around 10^{12} photons/sec).

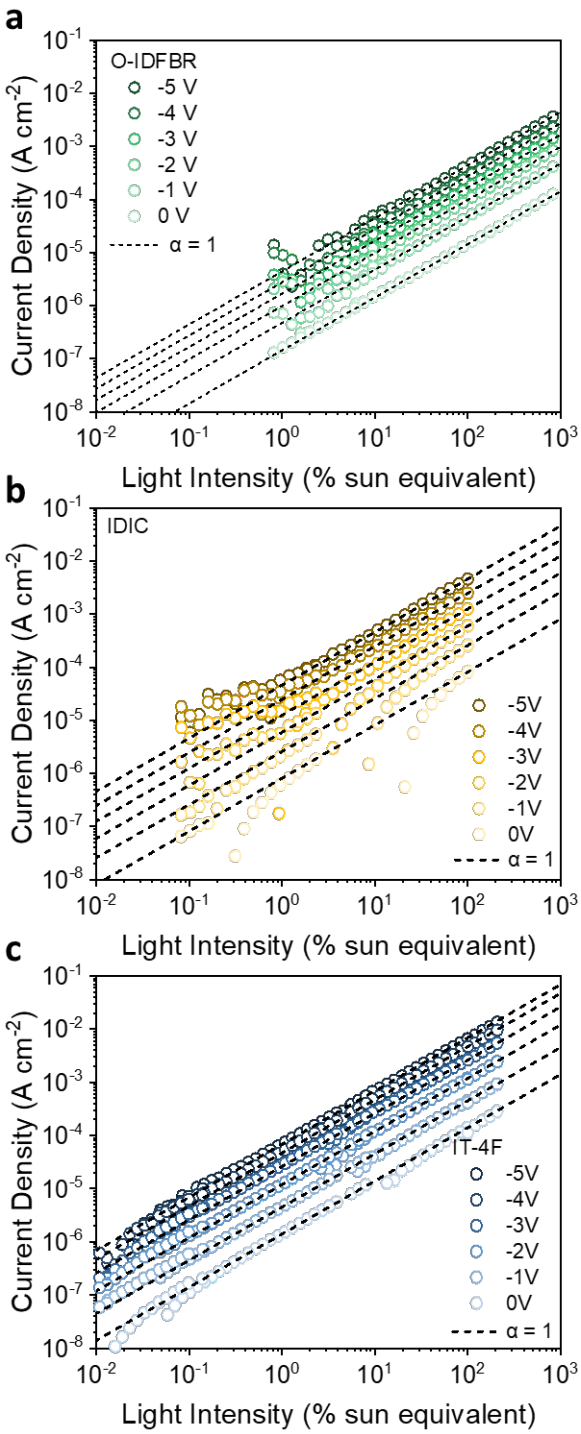

Supplementary Figure 12. Light intensity dependence on photocurrent density measured under various reverse bias condition for **a**, O-IDFBR and **b**, IDIC and **c**, IT-4F OPD devices.

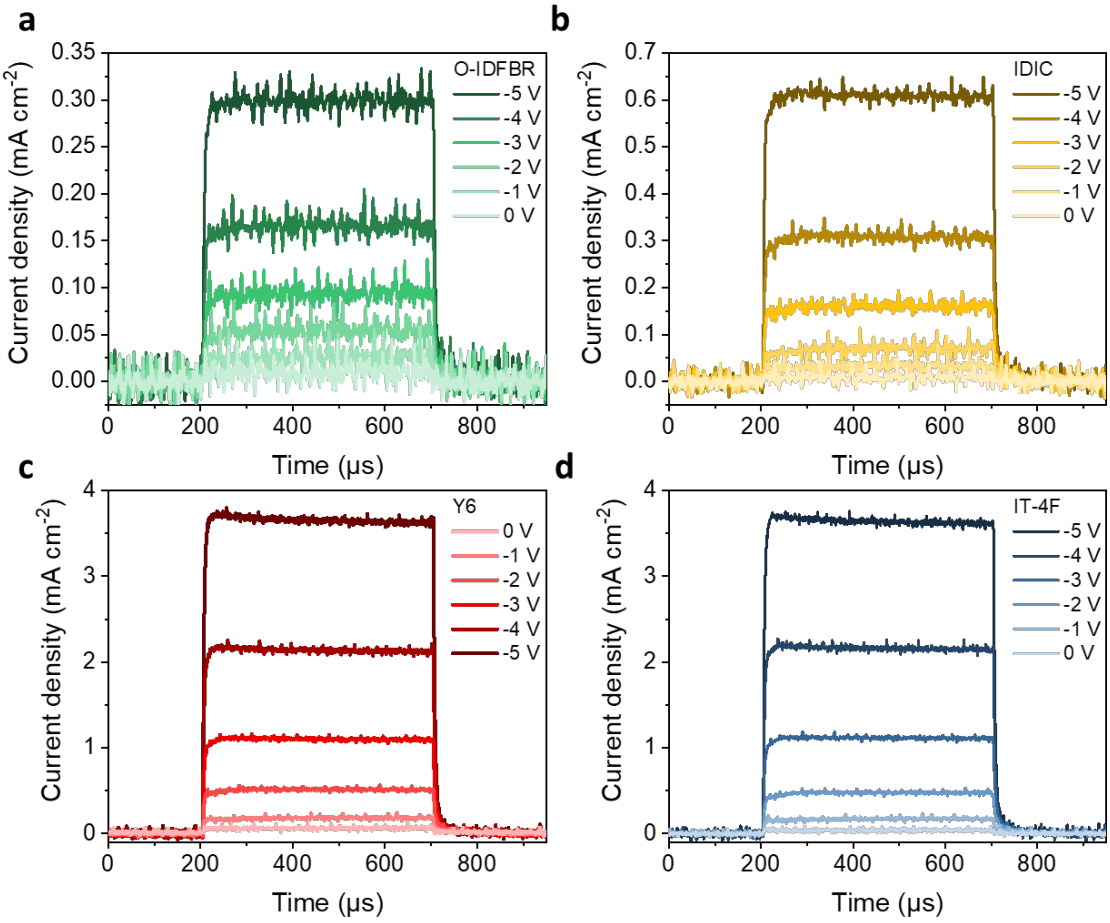

175

176 **Supplementary Figure 13.** Photocurrent transients with reverse bias from 0 to -5 V for **a**, O-
177 IDFBR, **b**, IDIC and **c**, IT-4F OPD devices, respectively. Similar to the bias EQE trends, the
178 rate of current increment is dependent on applied bias on molecule structure, with less increase
179 in O-IDFBR and IDIC devices (below 1 mA cm^{-2} even at -5 V) and greater increase in Y6 and
180 IT-4F devices (close to 4 mA cm^{-2} at -5 V).

181

182

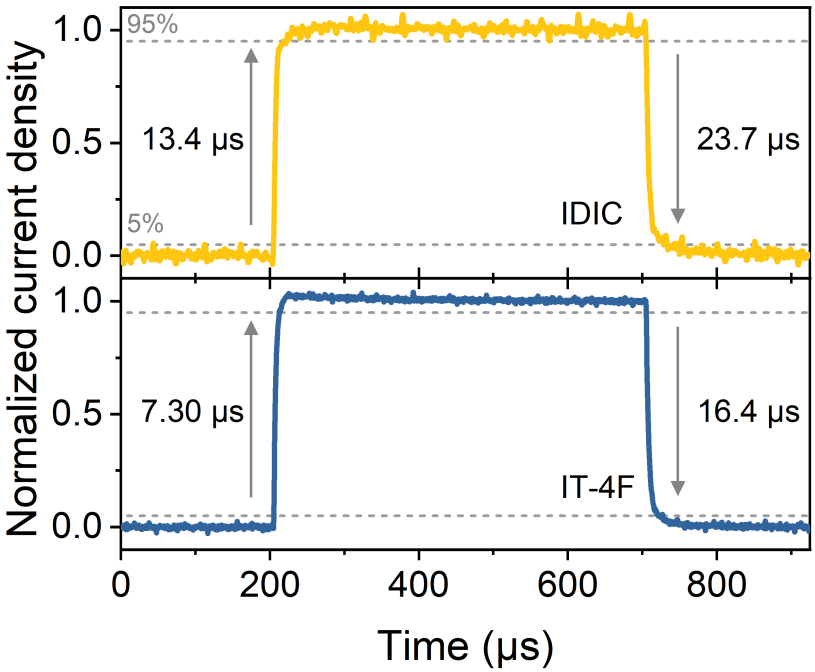

183

184 **Supplementary Fig. 14.** Normalized photocurrents of IDIC and IT-4F OPDs measured at -5
185 V bias condition (*f*=1 kHz). Red (633 nm) LEDs are used as an excitation light source.

186

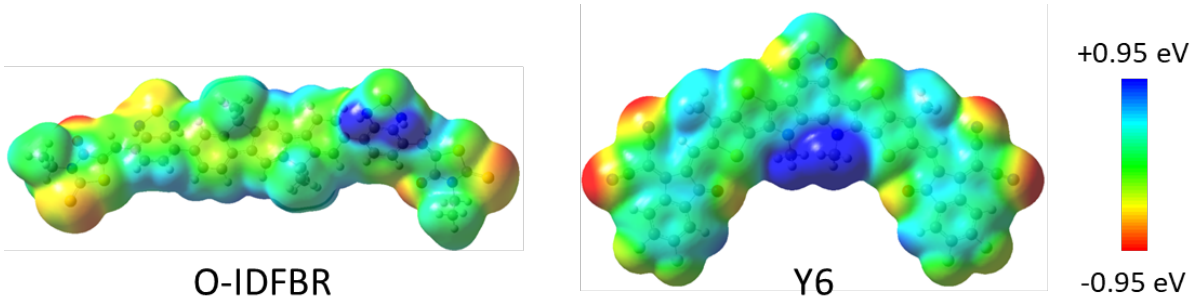

Supplementary Figure 15. a, Electrostatic maps of a monomer of O-IDFBR, IDIC, Y6 and IT-4F molecules. **b**, Calculated electrostatic potential (ESP) along the backbone of NFAs. It should be noted that Y6 has an additional benefit in terms of possibility of intermolecular interactions due to its five building blocks (*i.e.*, A-D-A-D-A) and its 3D-shaped structure[10]. Conversely, IDIC shows a relatively high ESP separation, but its linear backbone and small dimensions (only ≈26.5 Å compared to >30 Å for IT-4F) limit its overlapping with neighboring molecules.

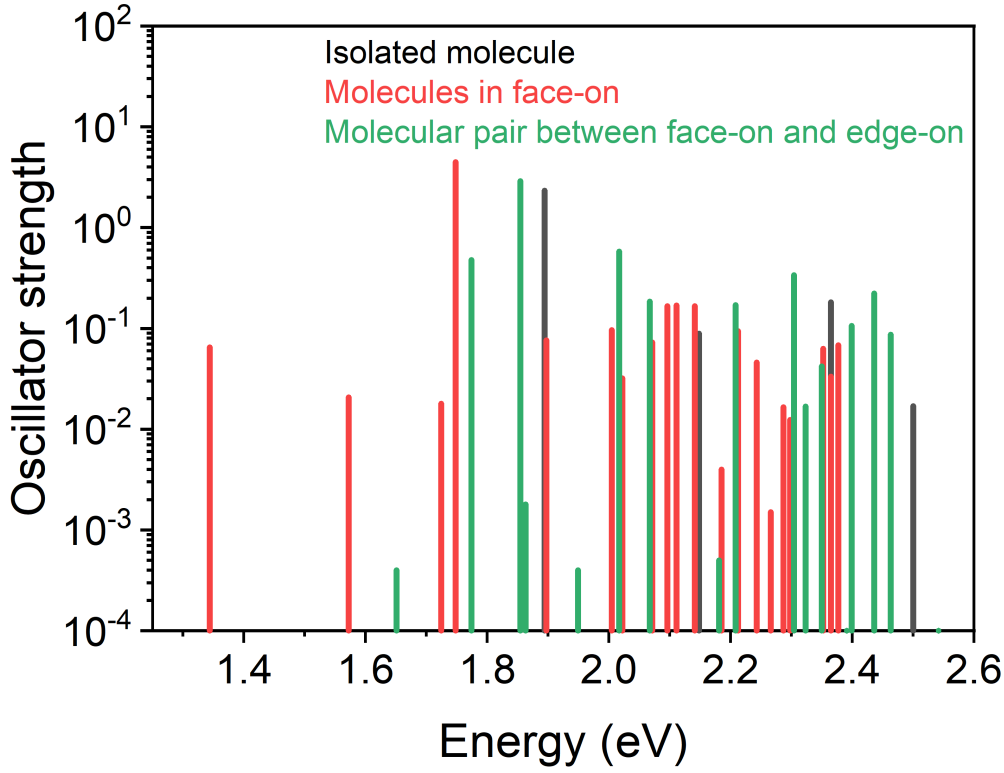

Supplementary Figure 16. Calculated oscillator strength of singlet excited states from S_1 to S_{20} for isolated molecule (black line), molecules in face-on (red line), molecules in edge-on (blue line), and molecular pair between face-on and edge-on (green line) in Y6.

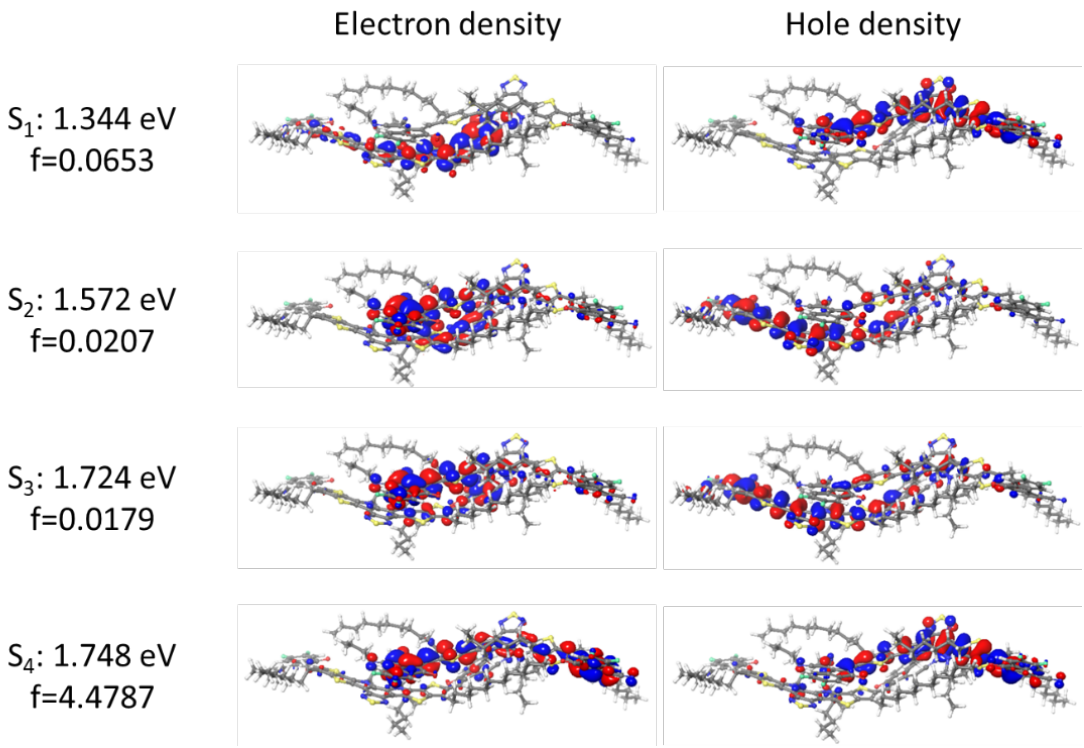

Supplementary Figure 17. Electron and hole density plots of 4 lowest-energy singlet excited states (S_1 to S_4) of two Y6 molecules with face-on packing.

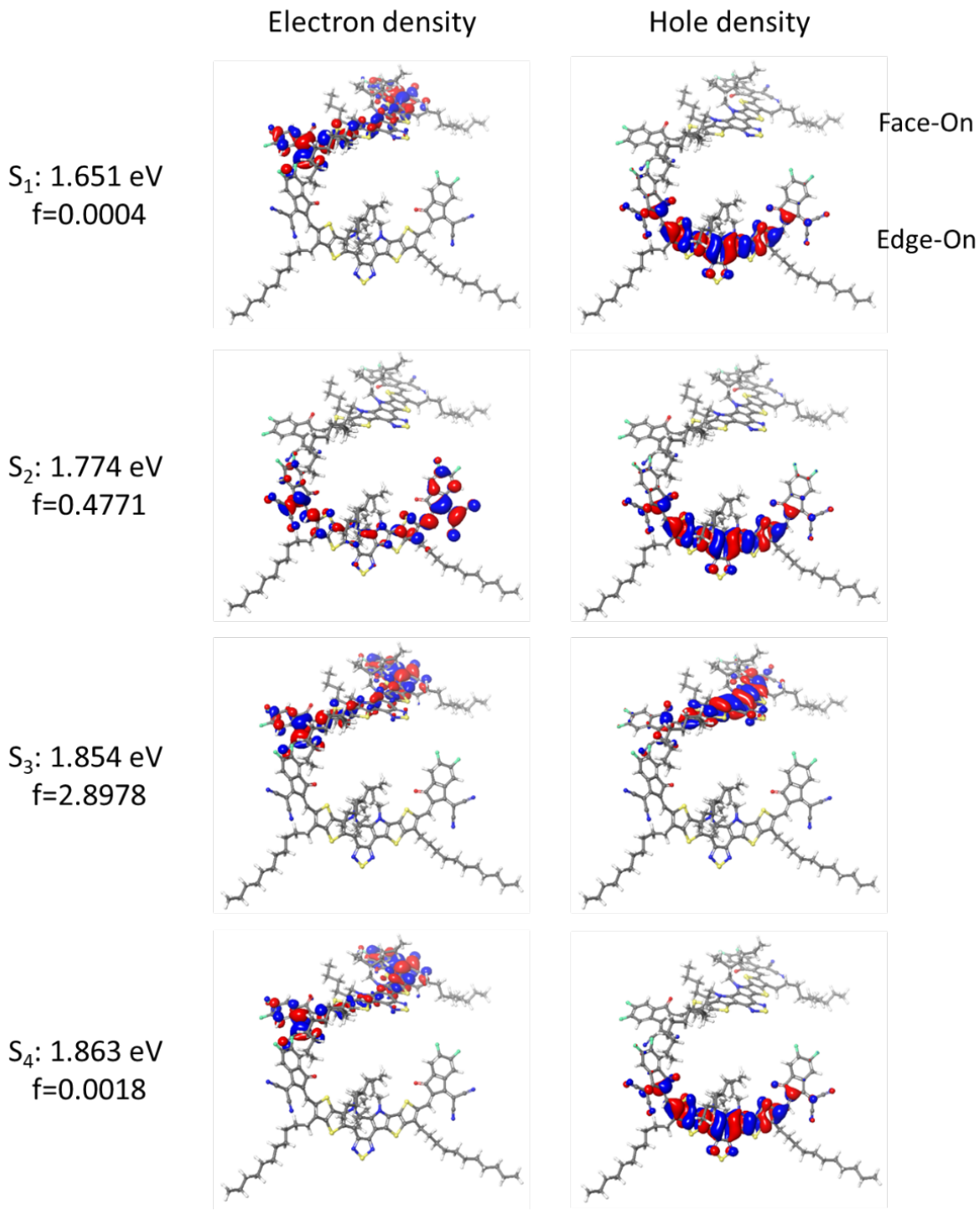

Supplementary Figure 18. Electron and hole density plots of 4 lowest-energy singlet excited states (S_1 to S_4) of orthogonally packed two Y6 molecules (see Supplementary Fig. 19 for details).

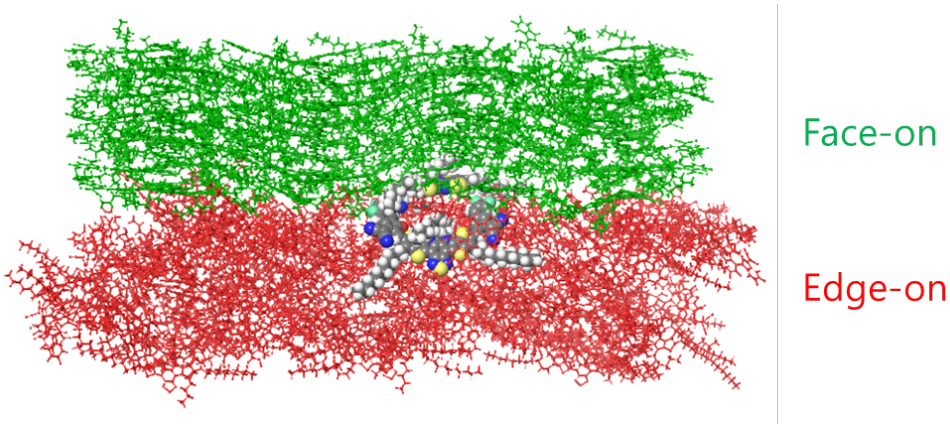

Supplementary Figure 19. Orthogonally packed two Y6 molecules (used in Supplementary Fig. 18) is extracted from the interface of face-on and edge-on packings.

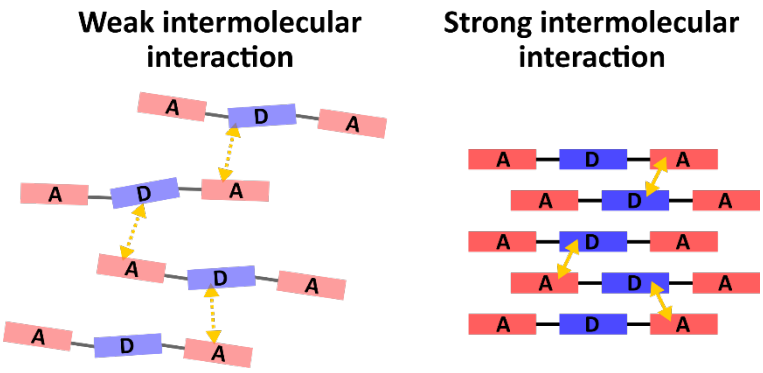

Supplementary Figure 20. Schematic images showing molecular packing in NFA films affected by molecular structure (twisted *vs*. planar) and strengths of intermolecular interaction either weak or strong.

Experimental evidence of CTE states and free charge generation

The generation of CTE states in single NFA systems is also confirmed by the surface photovoltage (SPV) measurement (**Supplementary Fig. 21**)[11,12]. SPV signals detected under weak light intensity illumination for IDIC and Y6 indicating existence of CTE states possibly followed by free charge generation even without applying external electric field. CTE states formed in IDIC and Y6 neat films can be separable into free charge carriers further by external electric field. Despite closely packed π-π stacking in IDIC film, charge generation and extraction properties under reverse bias differ from those of Y6. This is attributed to much lower Q_π in IDIC, inducing no energetic offset between crystallites. As for O-IDFBR, due to the absence of CTE characteristics, electric field induced charge generation efficiency cannot be comparable to the other NFAs.

We further compare EQE spectra with 2 types of Y6 devices; mostly face-on *vs.* mixed (face-on & edge-on) molecular orientation of Y6. To fabricate those devices, we referred a paper which shows a facile control of molecular orientation by changing solvents – CF for mostly face-on and CB for the mixed orientations[13]. As expected, Y6 device with the mixed orientation exhibits higher EQE compared to that of the mostly face-on Y6 device (**Supplementary Fig. 22**). This is clear evidence of efficient CTE states followed by free charge generation, enabled by high Q_π and differently oriented crystallites in NFA films.

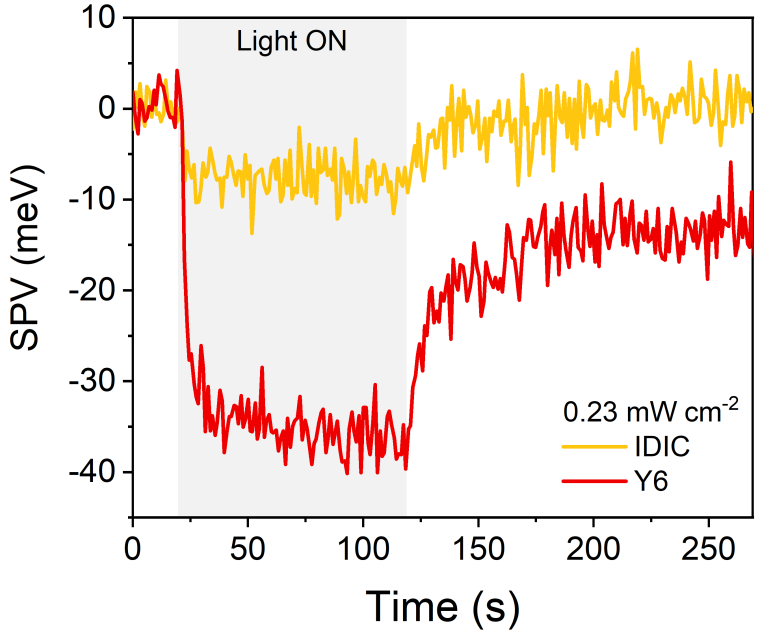

Supplementary Figure 21. Surface photovoltage signal for IDIC and Y6 films under low light illumination, showing the changes in contact potential difference between light and dark conditions between a Kelvin probe and the sample surface. Sample structure is Glass/ITO/ZnO/NFAs.

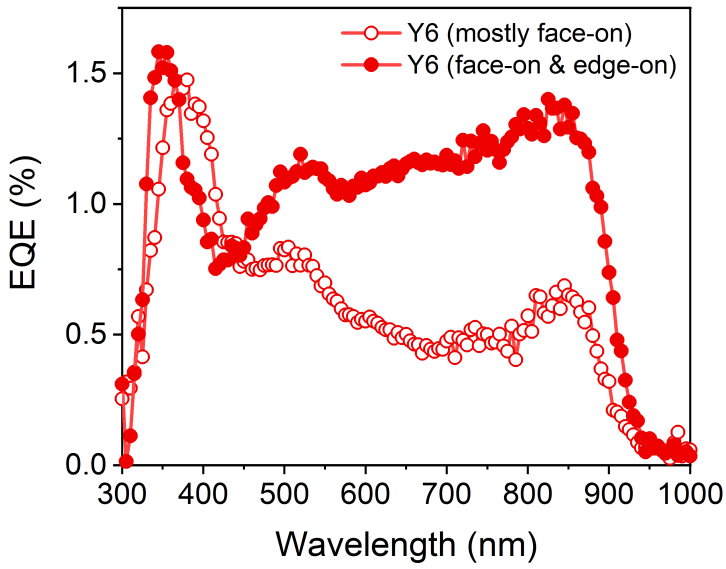

Supplementary Figure 22. EQE spectra of Y6 devices with different molecular orientations.

Supplementary Table 1. Summary of device parameters of NFA OPDs at -3 V of reverse bias applied.

Active layer	Thickness [nm]	EQE [%]	R [A W^{-1}]	J_d [A cm^{-2}]	D^* [Jones]
O-IDFBR	53	9.27	0.040	2.69×10^{-8}	4.32×10^{11}
IDIC	59	9.67	0.057	1.02×10^{-7}	3.17×10^{11}
Y6	53	22.1	0.151	9.51×10^{-9}	2.74×10^{12}
IT-4F	48	28.1	0.169	9.19×10^{-9}	3.11×10^{12}

Supplementary Table 2. Summarized figure of merits of reported OPD results

Device structure	J_d (A cm^{-2})	R (A W^{-1})	D* (Jones)	τ_{rise} (μs)	τ_{fall} (μs)	Ref.
ITO/ZnO/PTB7-Th:FOIC/ MoO_3/Ag	9×10^{-6} (-0.5 V)	0.45 (-0.1V)	2×10^{11} (-0.1 V)	-	0.4549 (under pulsed laser)	14
ITO/ZnO/PTB7-Th:CO1-4Cl/MoO_3/Ag	8×10^{-8} (-2 V)	0.50 (-0.1 V)	3.31×10^{13} (-0.1 V)	≥10	≥10	15
ITO/PEIE/ PCDTBT:PC_{60}BM/ PEDOT:PSS	3.1×10^{-10} (-2 V)	0.32 (-2.0 V)	3.21×10^{13} (-2 V)	7.7 (-2 V)	10.9 (-2 V)	16
Ag(Au)/PEIE/ PBTTT :PCBM/MoO_3/Ag	6×10^{-9} (-0.5 V)	0.27 (0 V)	$\sim10^{13}$ (0 V)	-	0.23 (0 V, under pulsed laser)	17
ITO/ZnO/PIF:IT-4F/MoO_3/Ag	10^{-7} (-5 V)	0.23 (-8 V)	6.9×10^{10} (-2)	~1 (-2 V)	-	18
ITO/TiO_2/poly-C_{60}/Cy7-T/MeO-TPD/MoO_3/Au/MoO_3	3.3×10^{-8} (-1 V)	0.15 (-2 V)	3×10^{12} (-0.1 V)		~1 (0 V, under pulsed lase)	19
ITO/Lys/ PBDTT-DPP:PB_{71}BM/ MoO_3/ Al	3.0×10^{-9} (-2 V)	0.12 (-2 V)	1.03×10^{14} (1 V)	0.289 (-1 V)	0.432 (-1 V)	20
Al/(Ca)/(C_{60})/p-DTS(FBTTh$_2$)$_2$:PC_{71}BM/ PEDOT:PSS/ITO	1.1×10^{-10} (-0.5 V)	0.39 (-0.5 V)	9.2×10^{12} (-0.5 V)	-	-	21
Al/PDPP3T:PC_{71}BM/ Poly-TPD or PEDOT:PSS/ITO	3.1×10^{-9} (-2 V)	0.21 (-1 V)	1.5×10^{13} (-0.5 V)	0.43 (-1 V)	0.31 (-1 V)	22
Al/C_{60}:LiF/PTB7-Th:IEICO-4F/ Poly-TPD/ITO	2.1×10^{-10} (-2 V)	0.45 (-2 V)	5.6×10^{13} (-2 V)	7.5 (-2 V)	9.2 (-2 V)	23
ITO/ ZnO/ PSBOTz:T2-OEHRH/ MoO_3/ Ag	7.1×10^{-10} (-2 V)	0.31 (-2 V)	2.04×10^{13} (-2 V)	30 (0 V)		24
ITO/PEDOT:PSS/PM6:O4TFIC/Phen-NaDPO/Ag	9×10^{-2} (-2 V)	0.5 (0 V)	9×10^{11} (0 V)	2.4 (-2 V)	3.7 (-2 V)	25
ITO/HTL/D18/Y6/ETL/Al	10^{-5} (-2 V)	0.5 (0 V)	1.39×10^{13} (0 V)	15 (0 V)	14 (0 V)	26
Al/LiF/PNIR :ITIC/PEDOT :PSS/ITO	6.1×10^{-8} (-0.5 V)	0.11 (-0.5 V)	$\sim10^{12}$ (-0.5 V)	51.7 (-0.5 V)	148.1 (-0.5 V)	27

Supplementary Table 3. Summary of photo-response time for all NFA OPDs measured under -5 V bias condition, comparing a time required for 80% change and 90% change of photocurrent.

NFA	80% change (10%↔90%)		90% change (5%↔95%)	
	τ_{rise} [μs]	τ_{fall} [μs]	τ_{rise} [μs]	τ_{fall} [μs]
O-IDFBR	11.7	10.9	14.9	26.0
IDIC	5.90	13.7	13.4	23.7
Y6	5.70	9.00	7.90	13.6
IT-4F	5.90	9.10	7.30	16.4

References

1. Kresse, G. & Furthmüller, J. Efficiency of ab-initio total energy calculations for metals and semiconductors using a plane-wave basis set. *Comput Mater Sci* **6**, 15–50 (1996).

2. Kresse, G. & Hafner, J. Norm-conserving and ultrasoft pseudopotentials for first-row and transition elements. *Journal of Physics: Condensed Matter* **6**, 8245–8257 (1994).

3. Kresse, G. & Hafner, J. Ab. initio molecular dynamics for liquid metals. *Phys Rev B* **47**, 558–561 (1993).

4. Kresse, G. & Joubert, D. From ultrasoft pseudopotentials to the projector augmented-wave method. *Phys Rev B* **59**, 1758–1775 (1999).

5. Kresse, G. & Furthmüller, J. Efficient iterative schemes for ab initio total-energy calculations using a plane-wave basis set. *Phys Rev B* **54**, 11169–11186 (1996).

6. Zhu, L. *et al.* Efficient Organic Solar Cell with 16.88% Efficiency Enabled by Refined Acceptor Crystallization and Morphology with Improved Charge Transfer and Transport Properties. *Adv Energy Mater* **10**, 1904234 (2020).

7. Zhu, W. *et al.* Crystallography, Morphology, Electronic Structure, and Transport in Non-Fullerene/Non-Indacenodithienothiophene Polymer:Y6 Solar Cells. *J Am Chem Soc* **142**, 14532–14547 (2020).

8. Bowers, K. J. *et al.* Scalable Algorithms for Molecular Dynamics Simulations on Commodity Clusters. in *Proceedings of the 2006 ACM/IEEE conference on Supercomputing* (Institute of Electrical and Electronics Engineers (IEEE), 2006). doi:10.1109/sc.2006.54.

9. Bochevarov, A. D. *et al.* Jaguar: A high-performance quantum chemistry software program with strengths in life and materials sciences. *Int J Quantum Chem* **113**, 2110–2142 (2013).

10. Zhang, G. *et al.* Delocalization of exciton and electron wavefunction in non-fullerene acceptor molecules enables efficient organic solar cells. *Nat Commun* **11**, (2020).

11. Labanti, C. *et al.* Light-intensity-dependent photoresponse time of organic photodetectors and its molecular origin. *Nat Commun* **13**, 3745 (2022).

12. Park, S. Y., Labanti, C., Luke, J., Chin, Y. C. & Kim, J. S. Organic Bilayer Photovoltaics for Efficient Indoor Light Harvesting. *Adv Energy Mater* **12**, (2022).

13. Zhu, L. *et al.* Efficient Organic Solar Cell with 16.88% Efficiency Enabled by Refined Acceptor Crystallization and Morphology with Improved Charge Transfer and Transport Properties. *Adv Energy Mater* **10**, (2020).

14. Liu, J. *et al.* Fast Response Organic Tandem Photodetector for Visible and Near-Infrared Digital Optical Communications. *Small* **17**, (2021).

15. Huang, J. *et al.* A High-Performance Solution-Processed Organic Photodetector for Near-Infrared Sensing. *Advanced Materials* **32**, (2020).

16. Kielar, M., Dhez, O., Pecastaings, G., Curutchet, A. & Hirsch, L. Long-Term Stable Organic Photodetectors with Ultra Low Dark Currents for High Detectivity Applications. *Sci Rep* **6**, (2016).

17. Tang, Z. *et al.* Polymer:Fullerene Bimolecular Crystals for Near-Infrared Spectroscopic Photodetectors. *Advanced Materials* **29**, (2017).

18. Strobel, N. *et al.* Color-Selective Printed Organic Photodiodes for Filterless Multichannel Visible Light Communication. *Advanced Materials* **32**, (2020).

19. Zhang, H. *et al.* Transparent organic photodetector using a near-infrared absorbing cyanine dye. *Sci Rep* **5**, (2015).

20. Nie, R. *et al.* Highly Sensitive and Broadband Organic Photodetectors with Fast Speed Gain and Large Linear Dynamic Range at Low Forward Bias. *Small* **13**, (2017).

21. Kim, I. K. *et al.* High-Performance, Solution-Processed Non-polymeric Organic Photodiodes. *Adv Opt Mater* **3**, 50–56 (2015).

22. Zhou, X., Yang, D. & Ma, D. Extremely Low Dark Current, High Responsivity, All-Polymer Photodetectors with Spectral Response from 300 nm to 1000 nm. *Adv Opt Mater* **3**, 1570–1576 (2015).

23. Yang, W. *et al.* Mitigating Dark Current for High-Performance Near-Infrared Organic Photodiodes via Charge Blocking and Defect Passivation. *ACS Appl Mater Interfaces* **13**, 16766–16774 (2021).

24. Kang, J. *et al.* Enhanced Static and Dynamic Properties of Highly Miscible Fullerene-Free Green-Selective Organic Photodetectors. *ACS Appl Mater Interfaces* (2021) doi:10.1021/acsami.1c02357.

25. Babics, M. *et al.* Non-fullerene-based organic photodetectors for infrared communication. *J Mater Chem C Mater* **9**, 2375–2380 (2021).

26. Wei, Y. *et al.* Self-Powered Organic Photodetectors with High Detectivity for Near Infrared Light Detection Enabled by Dark Current Reduction. *Adv Funct Mater* **31**, (2021).

27. Eun, H. J. *et al.* Effective Dark Current Suppression for High-Detectivity Organic Near-Infrared Photodetectors Using a Non-Fullerene Acceptor. *Cite This: ACS Appl. Mater. Interfaces* **13**, (2021).